Coupled Magnetic Nanostructures: Engineering Lattice Configurations

A. Talapatra,[1] and A. O. Adeyeye [1,2,a)]

[1]*Information Storage Materials Laboratory, Department of Electrical and Computer Engineering, National University of Singapore, Singapore 117576*

[2]*Department of Physics, Durham University, South Rd, Durham, DH1 3LE, UK*

[a)]*E-mail: adekunle.o.adeyeye@durham.ac.uk*

We present a systematic investigation of tunable magnetization dynamics of coupled magnetic nanostructures, arranged in one-dimensional arrays of horizontally and vertically coupled linear chains, and in two-dimensional arrays of square artificial spin ice lattice. The spatial distribution of the demagnetization field is markedly sensitive to the lattice arrangement, leading to a significant modification of the collective behavior of static and dynamic properties of the arrays. Using ferromagnetic resonance spectroscopy, the engineering of demagnetizing factors with various lattice arrangements has been established quantitatively. The signature of distinct spin wave modes, spatially localized in the constituent nanomagnets, were observed and tuned by the lattice arrangements and applied field orientation. The experimental results are well complemented with micromagnetic simulations.

The arrays of coupled nanomagnets (NMs) have shown multifaceted potential applications in the field of high-density patterned media[1], logic devices[2,3], and microwave filters with magnonic crystals.[4-6] The magnetization reversal in magnetic thin films is governed by energetics, primarily consisting of magnetocrystalline anisotropy, the exchange between neighboring spins, and magnetostatic energy. On the contrary, the shape anisotropy or the configurational anisotropy plays a key role to determine the magnetic behavior of a single nanostructure. The geometry of a NM is an important parameter to tune the demagnetization field which is directly proportional to the magnetization. Compared with non-interacting nanomagnets, magnetostatic interactions between the neighboring elements can lead to collective magnetic behavior with complex spin configurations and reversal processes. This effect becomes considerably important when the spacing between the neighboring NMs is less than the lateral dimensions of individual NM and results in the broadening of switching field distribution.[7-9] Thus, the geometry of a single NM and the lattice arrangements in an array dominate the collective static and dynamic magnetic properties. Magnetostatic interaction, being long-ranged in nature, enables the design of miniaturized magnetic devices using physically isolated but magnetostatically coupled NMs. The shape anisotropy is important in tuning the non-degenerate magnetic ground states, achieved by applying initializing fields in a specific direction for distinct magnetization dynamics.[10] The stacking sequence of the NMs also becomes a tuning factor of the effective magnetic anisotropy when the shape anisotropy is induced.[11] The reconfigurable microwave properties with bias-field-free operations have been shown with coupled rhomboid NMs,[12] demonstrating the spin wave transmission in arbitrary directions.[13] The change in periodicity and the direction of the stacking sequence in one-dimensional (1D) arrays of ellipsoid linear chains (LC) can also sculpt different remanent states due

to the change in magnetostatic interactions.[14,15] The dynamic properties of two-dimensional (2D) arrays of different geometries such as dot, triangle, ellipse, and ring have been extensively studied.[16-19] Interestingly, systematic control of spin wave mode cross-over and mode hopping with many-fold anisotropic behavior of spin wave frequencies under angular variation of the applied field have been reported for anti-dot lattices of different dimensions.[20] The role of magnetostatic interaction has also been established in terms of generating variable numbers of degenerate ground states leading to magnetic frustration using different artificial spin ice (ASI) or anti-ASI structures.[21-28] Moreover, the role of insertion of defects in the form of missing periodicity,[27] variations in thickness/width of a single component,[30,31] effect of transition from single-domain to vortex states with the increasing thickness (d)[32] and interactions in aperiodic structures[33] can selectively modify the magnetostatic environment of the arrays. A recent trend in studying the state of magnetization and its dynamics in 3D magnetic nanostructures has also been observed.[34,35]

In this letter, we investigate the role of configuration engineering on the magnetization dynamics of coupled arrays of ellipsoidal NMs, arranged in three distinct configurations, namely, 1D arrays of horizontally coupled linear chains (HLC) in which the neighboring elements are coupled along the major axis of the NMs, 1D arrays of vertically coupled linear chains (VLC) where the NMs are coupled along their minor axis, and 2D arrays of artificial square spin ice (SSI). Tunability of the collective behavior of static and dynamic magnetic properties is achieved by varying the lattice arrangements and the applied field orientations.

Periodic arrays of coupled magnetic nanostructures of three different configurations were fabricated over a large area (4 mm × 4 mm) on Silicon substrates using deep UV lithography[36] at an exposure wavelength of 193 nm. A 50 nm thick layer of Permalloy ($Ni_{80}Fe_{20,}$ Py) on top of a 5 nm thin Cr adhesive layer has been deposited over the corresponding resist patterns using electron beam evaporation, operating at a base pressure of 5×10^{-8} Torr with an optimized growth rate of 0.2 Å/s. Ultrasonic lift-off process with OK-73 resist-thinner was used for the complete removal of the photoresist. The completion of the lift-off process was assured from the scanning electron microscope (SEM) images, displaying the uniform distribution of ellipsoidal NMs over a large area in the configurations of HLC, VLC, and SSI as shown in Fig. 1 (a), (b), and (c) respectively. The corresponding insets display an enlarged view of the geometry. The lengths of the major axis (l) and minor axis (w) of individual NM are ~ 480 nm and 235 nm respectively with an error bar ~ 4%, maintaining the aspect ratio (l:w) around 2:1 for all the structures. The edge-to-edge distance between the consecutive NMs along the direction of the coupling is around 105 nm (s_l) for HLC and 52 nm (s_w) for VLC arrays. The separation between the NMs along the opposite of the coupling direction is large enough to neglect the magnetostatic interaction along that direction for Fig. 1 (a) and (b). The square unit cell of SSI is shown

as the inset of Fig. 1 (c) where the structure possesses a mirror symmetry along the diagonal of the square, as represented by the dotted line.

We have estimated the demagnetization field (H_d) for all the structures using object-oriented micromagnetic framework (OOMMF) codes.[37] The input parameters for the simulations include, saturation magnetization (M_s) = 800 emu/cm^3, exchange constant = 1.3 μerg/cm, damping constant = 0.008 with zero uniaxial anisotropy. Cubic cells, each of volume (5 nm)^3 were used to discretize the entire mask for simulation, adopted from the corresponding SEM images with the provision for applying 2D periodic boundary conditions. The saturated states for all the structures were first obtained by applying 2kOe of field along the *x*-axis and brought back to zero thereafter to initialize the remanent configurations. The 2D profiles for the spatial variation of H_d at the remanent states are depicted in Fig. 1 (d)-(f). For a detailed understanding, we have shown the line-profiles of the *x (y)* component of H_d ($H_{d\text{-}x(y)}$) along the *x(y)*-axis when the remanent state was achieved separately with the applied field along *x* (H_x) and *y* (H_y) axes. Comparing Fig. 1 (g) and (j) for HLC, it can be clearly seen that the maximum variation in $H_{d\text{-}x}$ ($\Delta H_{d\text{-}x}$) is smaller than $\Delta H_{d\text{-}y}$ which confirms that the x-axis is the direction of easy axis for the HLC arrays, as expected. From Fig. 1 (h) and (k), it can be clearly understood that $\Delta H_{d\text{-}x}$ is close to that of $\Delta H_{d\text{-}y}$ which suggests a strong competition between the shape anisotropy (along the *x*-axis) and magnetostatic interaction acting along the direction of coupling for the VLC arrays. For the SSI structures, the variation in $H_{d\text{-}x}$ and $H_{d\text{-}y}$ are shown in Fig. 1 (i) and (l) respectively at the remanent state achieved with H_x only. Both the line scans along the *x* and *y* axes depict the easy directions of the NMs, as shown by the dotted and solid lines respectively in Fig. 1 (f). The value of $\Delta H_{d\text{-}x}$ is found to be larger than $\Delta H_{d\text{-}y}$. Thus, the analysis of H_d along different directions highlights the magnetic interactions and the behavior of effective field inside the arrays of NMs with different lattice arrangements at remanent condition.

The collective magnetization reversal for the entire sample was characterized using a superconducting quantum interference device (SQUID) with the field applied in the plane of the samples. We have also investigated the magnetic ground states using magnetic force microscopy (MFM). Shown in Fig. 2 are the M-H loops for all the three configurations. For the HLC and VLC arrays, the hysteresis loops are shown along three different angles (φ) of H_{app} with respect to the direction of the major axis of the NMs (schematic is shown as the inset of Fig. 1 (a)). For φ = 0°, Fig. 2 (a) shows that HLC arrays reverse through a two-stage process, where the first switching occurs at 30 Oe followed by the final switching at -220 Oe. This multiple switching suggests that all the NMs do not switch simultaneously, probably due to the presence of various states of magnetization, resulting in the broadening of the switching field distribution. MFM at the remanent state (inset) depicts the presence of distorted single domain states (C or S state) and the presence of uniform, single vortex states. As a result of that, the vortex state reverses first and is followed by the switching of other states at the higher H_{app}. The density of vortex increases

for φ = 45° which results in a reduction of the squareness (ratio of remanent to saturation magnetization, M_R/M_s) to 56% compared to 77% for φ = 0°. As expected, the hysteresis loop is significantly different for φ = 90° due to the effects of shape anisotropy. The slanted loop with a higher nucleation field ~ 1 kOe suggests that the magnetization reversal is dominated by the nucleation, propagation, and annihilation of the vortices which can also be correlated with the MFM images. For the VLC arrays, magnetostatic interaction competes with the shape anisotropy as the coupling direction is opposite to that of the easy axis of the NMs. The hysteresis loops are slanted with negligible M_R/M_s and coercivity, as seen from Fig. 2 (b) where the nucleation field varies as 350, 380 and 650 Oe for φ = 0°, 45°, and 90° respectively. The presence of uniform, single vortex states at remanence is seen for all field angles. For the SSI arrays (Fig. 2 (c)), hysteresis loops are shown along φ = 0° and 45°. Multiple-step reversal around 950 and 270 Oe are observed for SSI along φ = 0° and almost linear decrease in magnetization below 300 Oe along φ = 45°. The MFM images of the SSI arrays depict the presence of single vortex and flux-closure patterns along both the directions of H_{app}, which can be attributed to the linear decrease in magnetization with negligible M_R/M_s by minimizing the net magnetic energy of the system.

We have investigated the magnetization dynamics using ferromagnetic resonance (FMR) spectroscopy with field sweep at a fixed frequency, varied in the range from 8 GHz to 16 GHz. The representative FMR spectra at 10 GHz are shown in Fig. 3 (a)-(c) as the derivative of absorbed power with respect to the applied field ($^{dP}/_{dH}$). The presence of the first fundamental mode with the highest intensity is observed at H_{a1} (0.57 kOe), H'_{a1} (0.97 kOe), and H''_{a1} (2.15 kOe) for φ = 0°, 45°, and 90° respectively for HLC arrays (Fig. 3 (a)). This is easy to understand that for any constant microwave frequency, the value of the resonance field (H_R) is lower along the easy axis compared to that along the hard axis, which requires an additional field to overcome the shape anisotropy. The fundamental mode corresponds to the power absorption at the center of the NMs. The FMR spectra for the VLC arrays in Fig. 3 (b) display the fundamental modes at H_{b1} (1.18 kOe), H'_{b1} (1.37 kOe), and H''_{b1} (1.59 kOe) for φ = 0°, 45°, and 90° respectively. By comparing the position of the modes for HLC and VLC arrays, it can be confirmed that φ = 0° is the easy axis for both the HLC and VLC arrays. However, $H_{a1} < H_{b1}$ indicates stronger effective anisotropy for the HLC arrays. The SSI arrays display two distinct FMR modes (Fig. 3 (c)) at H_{c1} (0.79 kOe), and H_{c2} (2.05 kOe). At φ = 0°, the horizontal NMs of the SSI arrays experience the field along the easy axis while the vertical NMs experience that along the hard axis. Thus, H_{c1}at a lower field value corresponds to the power absorption in the horizontal NMs and H_{c2} for the vertical NMs. The symmetry axis along 45° for the SSI structure results in similar in-plane demagnetization along the *x* and *y*-axis, which accounts for a single FMR mode at H'_{c1} (1.19 kOe) for φ = 45°. Further, the variation of FMR field and frequency is fitted with Kittel's formula,[38] $f_R = (\gamma/2\pi)\sqrt{[\{H_{x(y)} + (N_z - N_{x(y)}).4\pi M_s\}\{H_{x(y)} + (N_{y(x)} - N_{x(y)}).4\pi M_s\}]}$, where f_R, and

γ indicate the resonance (microwave) frequency, and gyromagnetic ratio respectively. Importantly, N_x, N_y, and N_z are the demagnetizing factors along the *x*, *y*, and *z* (along film thickness) axis and satisfies the relationship, $N_x + N_y + N_z = 1$. The Kittel fit (solid lines) of the FMR data (symbols) for φ = 0° are shown in Fig. 3 (d). The FMR data, obtained with H_{app} along the hard axis, fit with the Kittel formula only at the high field regime (not shown).[39] The best fits yield γ = 18.1 MHz/Oe and M_s ~ 795 emu/cm^3 for all the three structure which is commonly used for Py nanostructures.[20] The demagnetizing factors, estimated from the Kittel fits, are recorded in Table-1 and compared with those for a single ellipsoidal NM with *w*/*l* = 0.5, *d*/*l* = 0.1 (resembles close to the geometry of a single NM considered here), numerically calculated by Cronemeyer.[40] Thus, the experimental data clearly shows the engineering of demagnetizing factors by tuning the lattice arrangements of the ellipsoidal NMs.

Dynamic micromagnetic simulations (frequency sweep) were performed for a comprehensive understanding of the role of different symmetry arrangements of NMs, inter-element separation, and the direction of H_{app}. A single NM is first considered which shows f_R around 15 GHz and 9.6 GHz at a saturating H_{app} (2 kOe), applied along the *x* and *y*-axis respectively, as shown in Fig. 4 (a) and (b) where the insets display the space-frequency-resolved 2D FMR mode profiles (red and blue denote the maximum and minimum power absorption respectively). Now, the HLC and VLC arrays were considered with a variable edge-to-edge separation. Larger inter-element separation makes the magnetostatic interaction weaker and the HLC array behaves effectively like a single NM when $s_l \geq 300$ nm, as the value of f_R is close to that of single NM along both *x* and *y*-axis, following Fig. 4 (c). Similar behavior is also observed for VLC arrays at $s_w \geq 400$ nm (Fig. 4 (d)). The trend of variation of f_R with separation is the opposite for both arrays due to the difference in the coupling scheme between the neighboring NMs. Interestingly, Fig. 4 (d) shows that VLC arrays experience a spin reorientation transition at s_w ~ 50 nm where the direction of the effective magnetic anisotropy switches from *y* to *x*-axes.

Comparative simulated FMR spectra along with the 2D mode profiles for the three nanostructures are shown in Fig. 5. The presence of highly intense modes f_{a1} and f'_{a1} for HLC (Fig. 5 (a)), f_{b1} and f'_{b1} for VLC (Fig. 5 (b)) arrays, are observed for φ = 0° and 90° respectively where the absorption takes place at the center of the NMs. The difference between f_{a1} and f'_{a1} (5.8 GHz) is larger than that of f_{b1} and f'_{b1}(0.8 GHz) due to the stronger effective magnetic anisotropy of the HLC arrays. Shown in Fig. 5 (c) is the simulated FMR spectra of SSI arrays, indicating the appearance of modes at f_{c1}(15.6 GHz) and f_{c2} (10.4 GHz) which are localized in the horizontal and vertical NMs respectively for φ = 0°. Uniform FMR absorption in all the NMs of the SSI structure is observed at f'_{c1}(13 GHz) for φ = 45°. The simulation results are in good agreement with the experimental observations.

In summary, we have probed the static and dynamic behavior of coupled $Ni_{80}Fe_{20}$ NMs arranged in three distinct configurations. A significant variation in the magnetic properties is observed due to the modification of the internal demagnetization field because of the lattice arrangements. We have shown how magnetostatic coupling between the neighboring NMs can be used to tune the demagnetizing factors and consequently the resonance frequencies with associated mode profiles because of the configurational anisotropy. The experimental results are in good agreement with the micromagnetic modeling. Our work shows potential importance in the field of reconfigurable magnonic crystals and microwave filter applications.

ACKNOWLEDGMENTS

This work was supported by the Ministry of Education, Singapore Tier 2 funding via grant number: R-263-000-C61-112. Dr. Navab Singh is thanked for the DUV templates. Dr. Dheeraj Kumar is acknowledged for fruitful discussions. The authors acknowledge Hitachi High-Tech Singapore Pte Ltd. for the Hitachi Regulus 8230 SEM facility at National University of Singapore. AOA would like to acknowledge the funding from the Royal Society and Wolfson Foundation.

DATA AVAILABILITY

The data that support the findings of this study are available from the corresponding author upon reasonable request.

REFERENCES

[1]T. R. Albrecht, H. Arora, V. Ayanoor-Vitikkate, J.-M. Beaujour, D. Bedau, D. Berman, A. L. Bogdanov, Y-A. Chapuis, J. Cushen, E. E. Dobisz, G. Doerk, H. Gao, M. Grobis, B. Gruney, W. Hanson, O. Hellwig, T. Hirano, P.-O. Jubert, D. Kercher, J. Lille, Z. Liu, C. M. Mate, Y. Obukhov, K. C. Patel, K. Rubin, R. Ruiz, M. Schabes, L. Wan, D. Weller, T.-W. Wu and E. Yang, Bit-patterned magnetic recording: theory, media fabrication, and recording performance, *IEEE Trans. Magn.* **51**, 0800342 (2015).

[2]H. Arava, N. Leo, D. Schildknecht, J. Cui, J. Vijayakumar, P. M. Derlrt, A. Kleibert, and L. J. Heyderman, *Phys. Rev. Appl.* **11**, 054086 (2019).

[3]A. Haldar, and A. O. Adeyeye, *ACS Nano* **10**, 1690 (2016).

[4]A. V. Sadovnikov, V. A. Gubanov, S. E. Sheshukova, Y. P. Sharaevskii, and S. A. Nikitov, *Phys. Rev. Appl.* **9**, 051002 (2018).

[5]A. Barman, S. Mondal, S. Sahoo, and A. De, *J. Appl. Phys.* **128**, 170901 (2020).

[6]A. V. Chumak, A. A. Serga, and B. Hillebrands, *J. Phys. D: Appl. Phys.* **50**, 244001 (2017).

[7]B. Pfau, C. M. Günther, E. Guehrs, T. Hauet, H. Yang, L. Vinh, X. Xu, D. Yaney, R. Rick, S. Eisebitt, and O. Hellwig, *Appl. Phys. Lett.* **99**, 062502 (2011).

[8]B. Pfau, C. M. Günther, E. Guehrs, T. Hauet, T. Hennen, S. Eisebitt, and O. Hellwig, *Appl. Phys. Lett.* **105**, 132407 (2014).

[9]T. Hauet, L. Piraux, S. K. Srivastava, V. A. Antohe, D. Lacour, M. Hehn, F. Montaigne, J. Schwenk, M. A. Marioni, H. J. Hug, O. Hovorka, A. Berger, S. Mangin, and F. A. Araujo, *Phys. Rev. B* **89**, 174421 (2014).

[10]A. Haldar, and A. O. Adeyeye, *Appl. Phys. Lett.* **108**, 162401 (2016).

[11]A. Talapatra, and A. O. Adeyeye, *Nanoscale* **12**, 20933 (2020).

[12]A. Haldar, and A. O. Adeyeye, *J. Appl. Phys.* **128**, 240902 (2020).

[13]A. Haldar, D. Kumar, and A. O. Adeyeye, *Nat. Nanotechnol.* **11**, 437 (2016).

[14]S. Jain, A. O. Adeyeye, and N. Singh, *Nanotechnology* **21**, 285702 (2010).

[15]D. Bisero, P. Cremon, M. Madami, M. Sepioni, S. Tacchi, G. Gubbiotti, G. Carlotti, A. O. Adeyeye, N. Singh, and S. Goolaup, *J. Nanopart. Res.* **13**, 5691 (2011).

[16]B. K. Mahato, B. Rana, D. Kumar, S. Barman, S. Sugimoto, Y. Otani, and A. Barman, *Appl. Phys. Lett.* **105**, 012406 (2014).

[17]G. Gubbiotti, M. Madami, S. Tacchi, G. Carlotti, H. Tanigawa, T. Ono, L. Giovannini, F. Montoncello, and F. Nizzoli, *Phys. Rev. Lett.* **97**, 247203 (2006).

[18]S. Jung, B. Watkins, L. DeLong, J. B. Ketterson, and V. Chandrasekhar, *Phys. Rev. B.* **66**, 132401 (2002).

[19]G. N. Kakazei, P. E. Wigen, K. Yu. Guslienko, R. W. Chantrell, N. A. Lesnik, V. Metlushko, H. Shima, K. Fukamichi, Y. Otani, and V. Novosad, *J. Appl. Phys.* **93**, 8418 (2003).

[20]S. Choudhury, S. Majumdar, S. Barman, Y. C. Otani and A. Barman**,** *Phys. Rev. Appl.* **10**, 064044 (2018).

[21]L. J. Heyderman and R. L. Stamps, *J. Phys.: Condens. Matter* **25**, 363201 (2013).

[22]S. Zhang, Dissertation, *Tuning geometries and interactions of artificial frustrated nanomagnets*, The Pennsylvania State University, USA, 2013.

[23]R. F. Wang, C. Nisoli, R. S. Freitas, J. Li, W. McConville, B. J. Cooley, M. S. Lund, N. Samarth, C. Leighton, V. H. Crespi and P. Schiffer, *Nature* **439**, 303 (2006).

[24]S. Ladak, D. E. Read, G. K. Perkins, L. F. Cohen and W. R. Branford, *Nat. Phys.* **6**, 359 (2010).

[25]I. Gilbert, Y. Lao, I. Carrasquillo, L. O'Brien, J. D. Watts, M. Manno, C. Leighton, A. Scholl, C. Nisoli and P. Schiffer, *Nat. Phys.* **12**, 162 (2016).

[26]J. Sklenar, Y. Lao, A. Albrecht, J. D. Watts, C. Nisoli, G-W. Chern and P. Schiffer, *Nat. Phys.* **15**, 191 (2019).

[27]Y. Li, G. W. Paterson, G. M. Macauley, F. S. Nascimento, C. Ferguson, S. A. Morley, M. C. Rosamond, E. H. Linfield, D. A. MacLaren, R. Maêedo, C. H. Marrows, S. McVitie and R. L. Stamps, *ACS Nano* **13**, 2213 (2019).

[28]X. Zhou, G.-L. Chua, N. Singh and A. O. Adeyeye, *Adv Funct. Mater.* **26**, 1437 (2016).

[29]J. Drisko, T. Marsh and J. Curnings, *Nat. Commun.* **8**, 14009 (2017).

[30]A. Farhan, M. Saccone, C. F. Petersen, S. Dhuey, R. V. Chopdekar, Y-L. Huang, N. Kent, Z. Chen, M. J. Alava, T. Lippert, A. Scholl and S. van Dijken, *Sci. Adv.* **5**, eaav6380 (2019).

[31]T. Dion, D. M. Arroo, K. Yamanoi, T. Kimura, J. C. Gartside, L. F. Cohen, H. Kurebayashi and W. R. Branford, *Phys. Rev. B* **100**, 054433 (2019).

[32]A. Talapatra, N. Singh and A. O. Adeyeye, *Phys. Rev. Appl.* **13**, 014034 (2020).

[33]M. Saccone, A. Scholl, S. Velten, S. Dhuey, K. Hofhuis, C. Wuth, Y-L. Huang, Z. Chen, R. V. Chopdekar and A. Farhan, *Phys. Rev. B* **99**, 224403 (2019).

[34]C. Donnelly, S. Finizio, S. Gliga, M. Holler, A. Hrabec, M. Odstrčil, S. Mayr, V. Scagnoli, L. J. Heyderman, M. Guizar-Sicairos, and J. Raabe, *Nat. Nanotechnol.* **15**, 356 (2020).

[35]S. Sahoo, S. Mondal, G. Williams, A. May, S. Ladak, and A. Barman, *Nanoscale* **10**, 9981 (2018).

[36]A. O. Adeyeye and N. Singh, *J. Phys. D: Appl. Phys.* **41**, 153001 (2008).

[37]M. Donahue, D. G. Porter, *OOMMF User's Guide*, Version 1.0, Intergency Report NISTIR 6376 (National Institute of Standard and Technology, Gaithersburg, MD) http://math.nist.gov/oommf.

[38]C. Kittel, *Phys. Rev.* **73**, 155 (1948).

[39]A. Ghosh, F. Ma, J. Lourembam, X. Jin, R. Maddu, Q. J. Yap, and S. T. Lim, *Nano Lett.* **20**, 109 (2020).

[40]D. C. Cronemeyer, *J. Appl. Phys.* **70**, 2911 (1991).

TABLE

Table-1: The estimated values of the demagnetizing factors for a single ellipsoidal NM (Cronemeyer's calculation) and the HLC, VLC, SSI arrays (from Kittel fit).

Demagnetizing factors	**Single NM**	**HLC**	**VLC**	**SSI**
N_x	0.0544	0.0484	0.0787	0.0505
N_y	0.1462	0.138	0.1025	0.1119
N_z	0.7995	0.8136	0.8188	0.8376

FIGURES

Figure 1

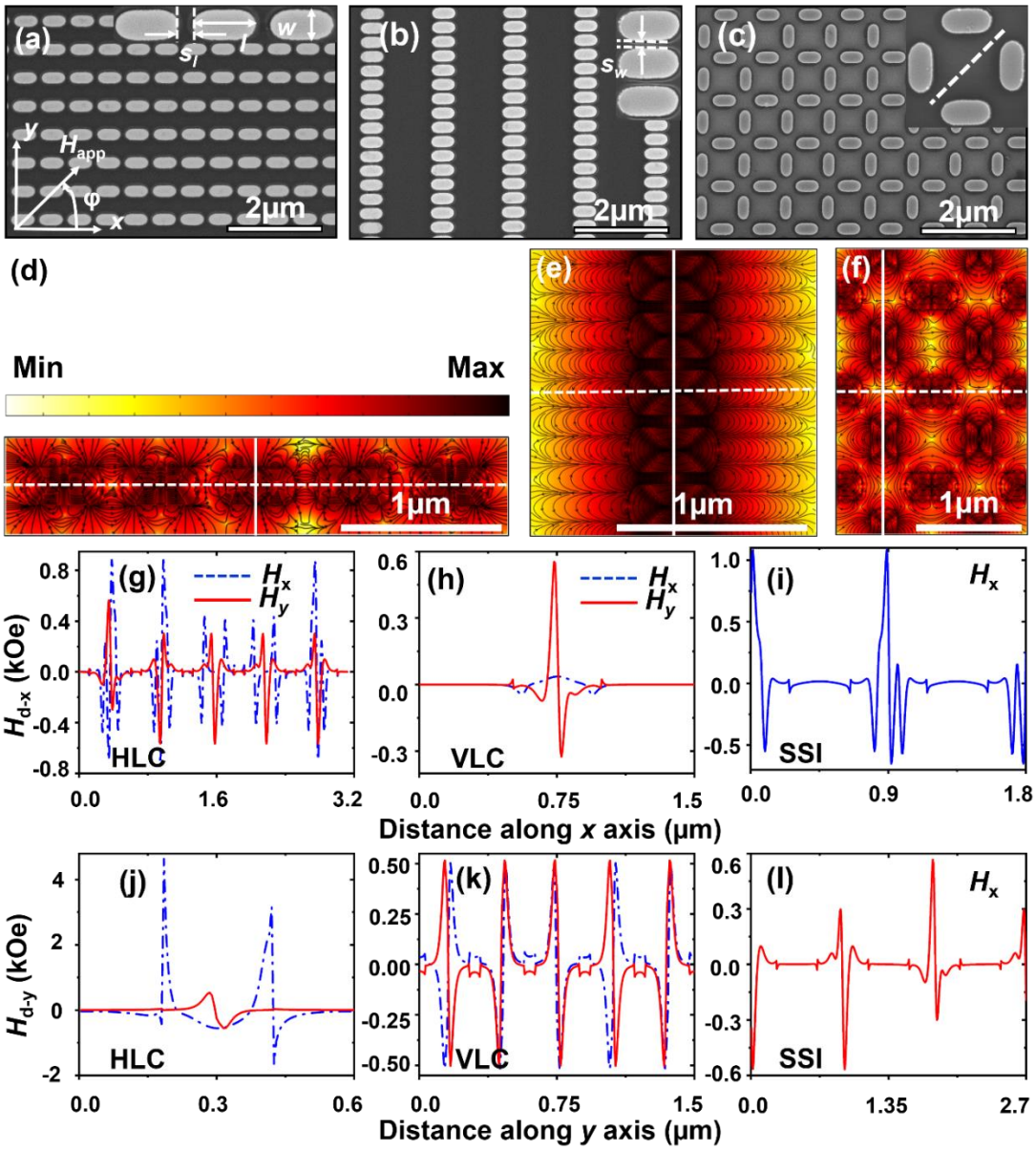

Fig.1: SEM images of (a) HLC, (b) VLC, and (c) SSI arrays, (d)-(f) represent the 2D profile of the spatial distribution of H_d, (g)-(i) represent the plots of the spatial variation of $H_{d\text{-}x}$ along the *x*-axis and, (j)-(l) represent the plots of the spatial variation of $H_{d\text{-}y}$ along the *y*-axis for the corresponding structures. The insets in the SEM images depict the magnified views. The dotted and solid lines in (d)-(f) are the guide to the eyes along which the $H_{d\text{-}x}$ and $H_{d\text{-}y}$ profiles are shown respectively. The colour bar is identical for all the images in (d)-(f). Note that the *x* and *y* components of H_d are plotted along the *x* and *y*-axis respectively.

Figure 2

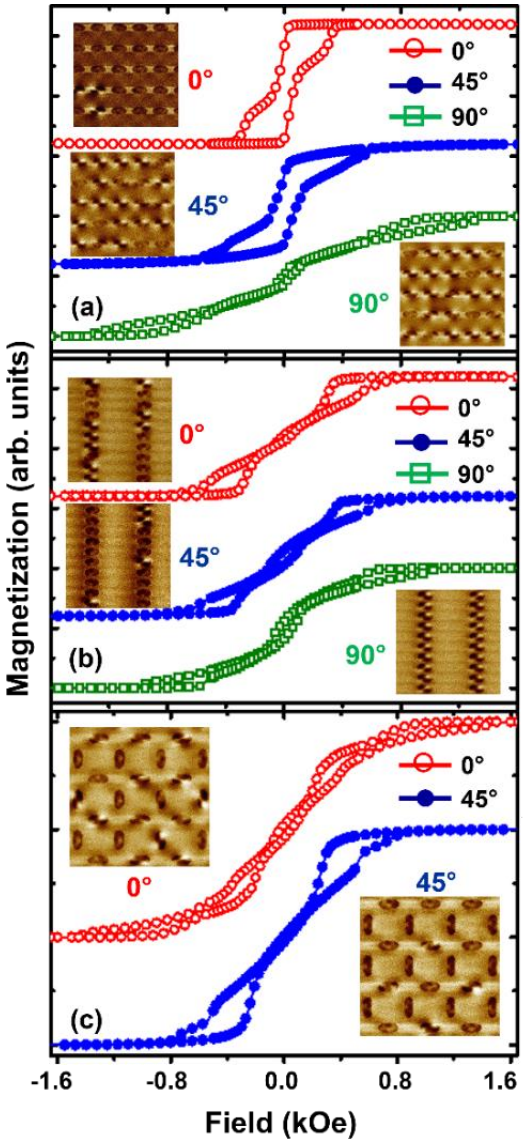

Fig.2: Hysteresis loops at different applied field angles with the corresponding spin states at remanence as insets for (a) HLC, (b) VLC, and (c) SSI arrays. All the MFM images are of dimensions 3μm × 3μm.

Figure 3

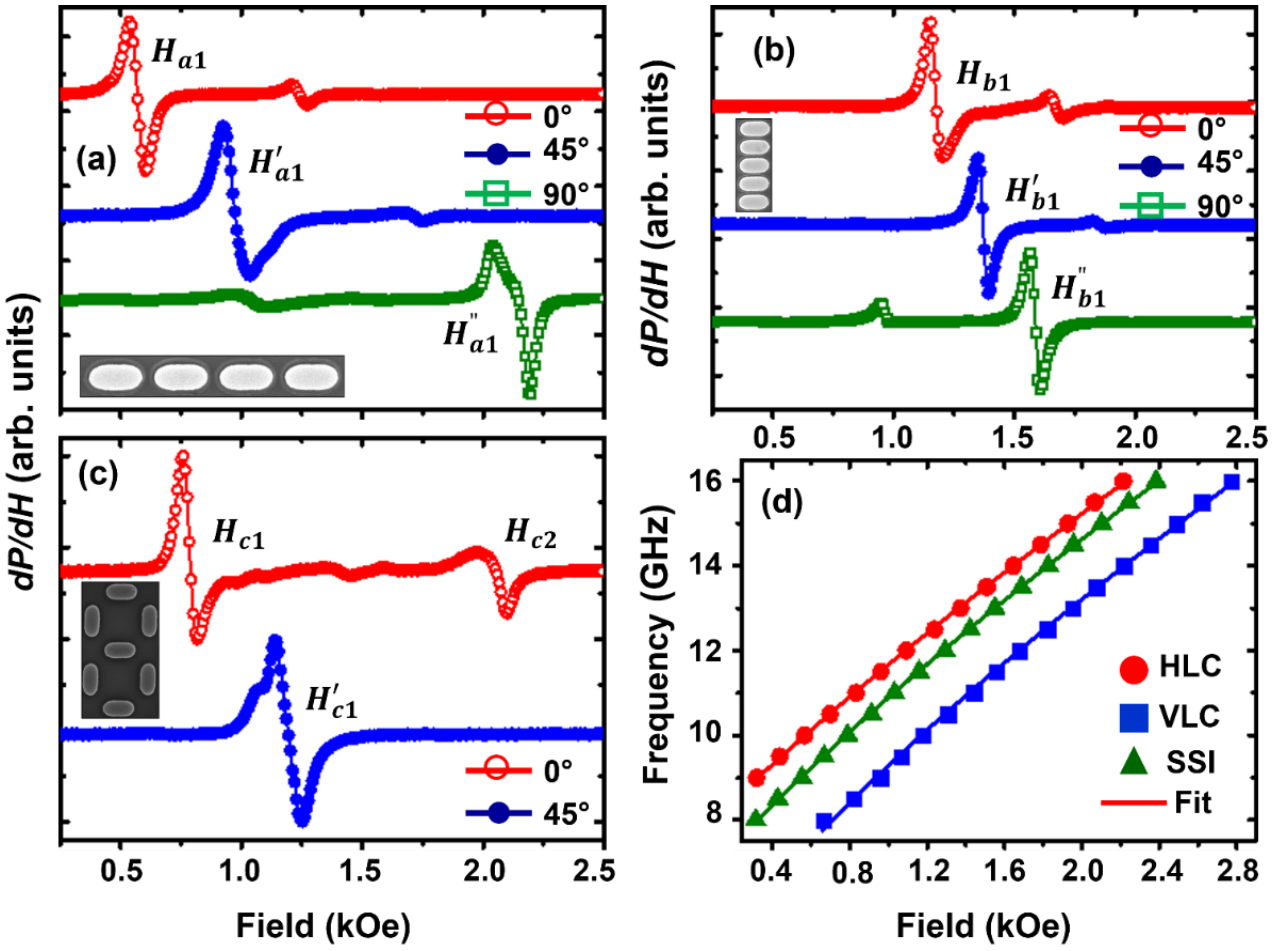

Fig.3: FMR spectra at a frequency of 10 GHz for (a) HLC, (b) VLC, and (c) SSI arrays (structures are shown as insets) with (d) the Kittel fit of the FMR field versus frequency variation for φ = 0°. For SSI, the fit for the variation of H_{c1} is shown.

Figure 4

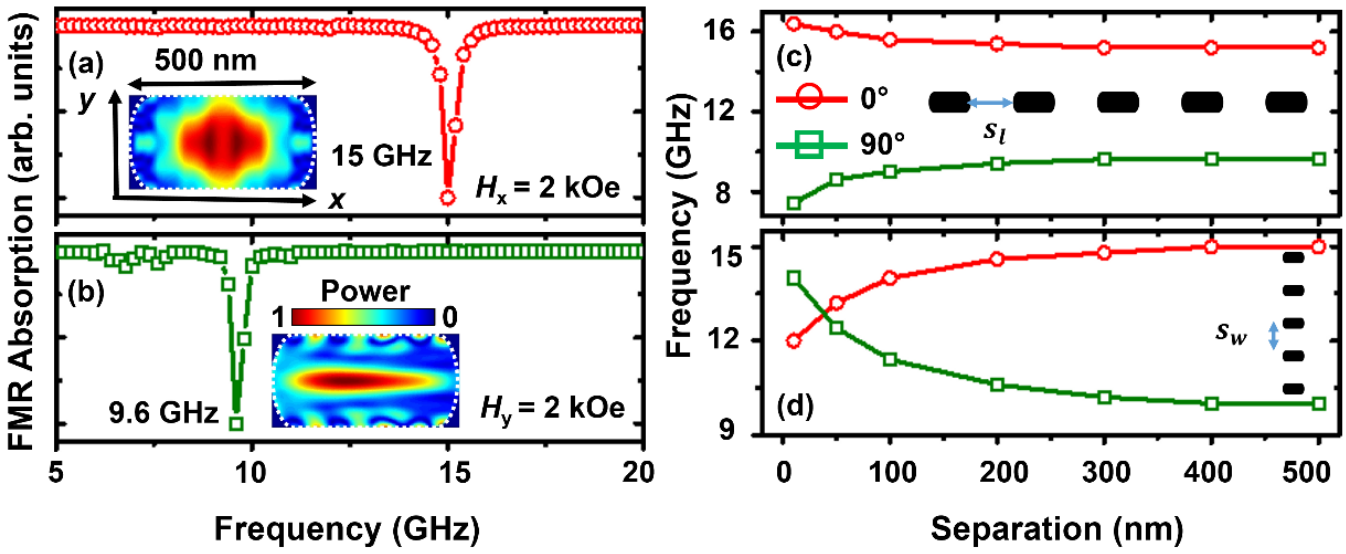

Fig.4: Simulated FMR spectra for a single nanomagnet at H_{app} = 2 kOe, applied along (a) *x*, and (b) *y*-axis. The insets (with identical scale bar and colorbar) display the 2D mode profiles (normalized) at the resonance frequency. The variation of FMR frequency is shown as a function of inter-dot separation for (c) HLC, and (d) VLC arrays.

Figure 5

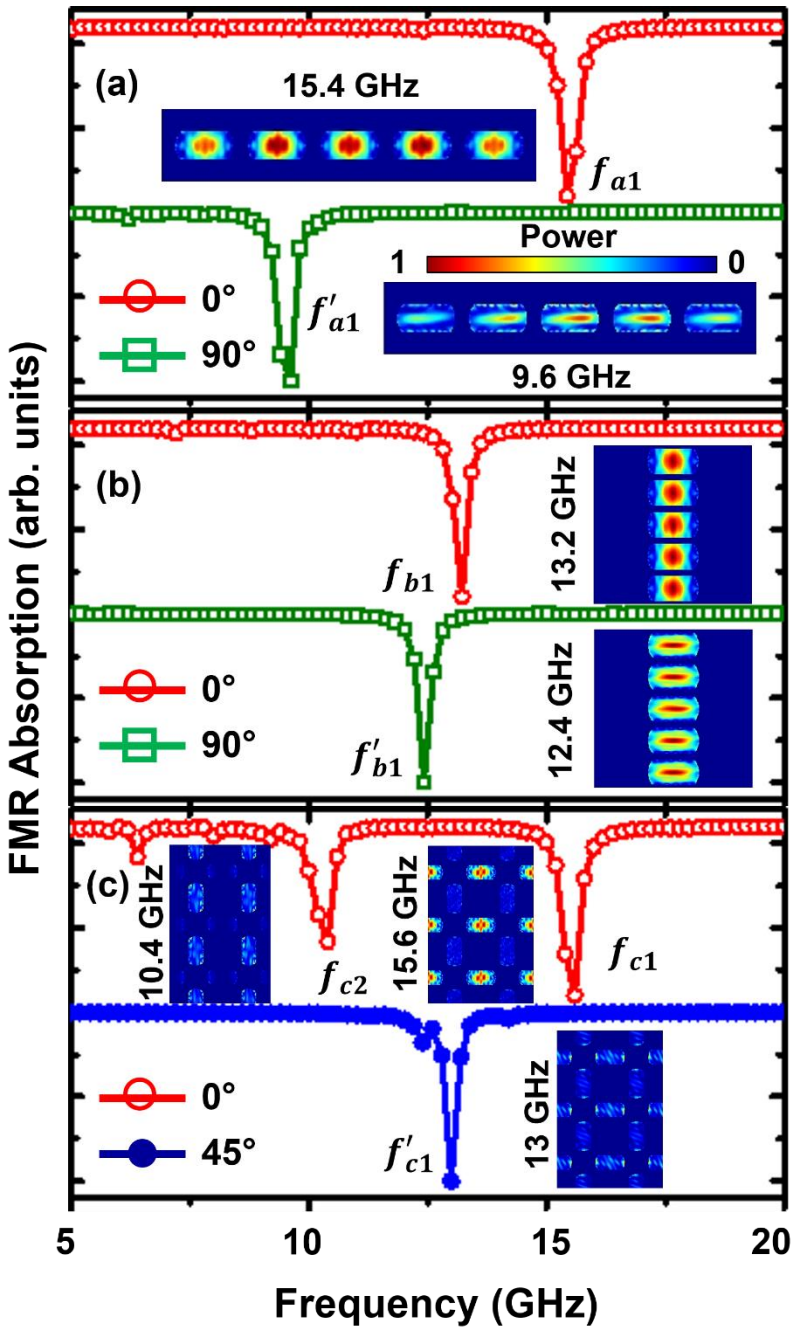

Fig.5: Simulated FMR spectra at H_{app} = 2 kOe, applied along different orientations for (a) HLC, (b) VLC, and (c) SSI arrays. The 2D mode profiles (normalized) corresponding to the resonance frequencies are shown as insets. The areas of simulations for (a), (b), and (c), are 3.12 μm × 0.6 μm, 1.5 μm × 1.5 μm, and 1.8 μm × 2.7 μm, respectively.